Eur. Phys. J. D **5**, 97–106 (1999)

THE EUROPEAN PHYSICAL JOURNAL D

EDP Sciences

Ultrafast photoelectron spectroscopy: Femtosecond pump-probe coincidence detection of ammonia cluster ions and electrons

V. Stert, W. Radloff[a], C.P. Schulz, and I.V. Hertel[b]

Max-Born-Institut für Nichtlineare Optik und Kurzzeitspektroskopie, Rudower Chaussee 6, 12489 Berlin-Adlershof, Germany

Received: 28 May 1998 / Received in final form: 31 August 1998 / Accepted: 7 September 1998

Abstract. A new type of experiment is described, in which the femtosecond pump-probe method is combined with the photoelectron-photoion coincidence technique and time-of-flight photoelectron energy analysis. The experimental conditions for observing true coincidences are discussed. The performance of the new time resolved, ultrafast photoelectron spectroscopy is exemplified by studying the excited state dynamics of ammonia molecules and clusters.

PACS. 36.40.Qv Stability and fragmentation of clusters – 42.65.Re Ultrafast processes; optical pulse generation and pulse compression

1 Introduction

In recent years, due to improved flexibility of femtosecond laser systems with extended tunability and sufficient pulse energy the direct study of ultrafast dynamics in excited states of free molecules and clusters has become more and more routine (see, *e.g.* [1]). In typical experiments, pump-probe techniques are used to ionize the molecules and clusters by two ultrafast laser pulses delayed in time with respect to another. The pump photon (energy $h\nu_1$) excites the system into the state of interest, its evolution with time being probed by the delayed ionizing photon (energy $h\nu_2$). The dependence of the ion signal on the delay time τ reflects the excited state dynamics. It does, however, give no direct information on the internal energy of the cluster ions after the ionization process since the excess energy $E_{exc} = h\nu_1 + h\nu_2 - IP$ (above the ionization potential IP) is shared among the internal energy of the ion, E_{ion}, and the kinetic energy of the detached electron, E_{el}. The Franck-Condon factors between the initially excited neutral cluster state and the final rovibrational states of the cluster ion determine E_{ion}(and hence E_{el}). Thus, both may change as the excited state develops with time and by measuring the photoelectron kinetic energy for each individual ionization process one may glean information on the internal ion energy from the experiment:

$$E_{ion}(\tau) = h\nu_1 + h\nu_2 - IP - E_{el}(\tau). \qquad (1)$$

If, in addition, the Franck-Condon factors are known, one may even infer information on the internal energy of the primarily excited neutral cluster states and their evolution with time. It is this kind of ultrafast dynamics driving the photochemistry of molecular excited states which one would like to understand – eventually in quantum chemical terms.

Very recently, femtosecond pump-probe PES has been used for negatively charged molecules and clusters [2]. For neutral excited species, to our knowledge only a single experiment has been reported so far studying ultrafast internal conversion in 1, 3, 5-hexatriene [3] by photoelectron spectroscopy (PES), using 200 fs laser pulses. On a somewhat longer time scale, photoelectron spectra of the ammonia molecule from two-color (2+1′) REMPI with picosecond lasers have been reported [4]. The ammonia molecule is excited to vibrational levels of the higher electronic $\tilde{B}$ and $\tilde{C}'$ states which are characterized by lifetimes above 7 ps. In all three cases the pump-probe measurements carried out with two different wavelengths allow an unambiguous correlation between the electrons and ions detected, since they originate from one well-defined process only.

In contrast, when studying the photoionization of neutral clusters, we have a distribution of cluster sizes in the target cluster beam and, moreover, the final products may fragment so that electrons and ions observed can arise from a variety of different processes. In order to obtain the kind of information discussed above, such experiments require in this case simultaneous detection of ions and electrons with analysis of the electron kinetic energy, *i.e.* coincidence techniques have to be used.

[a] e-mail: radloff@mbi-berlin.de

[b] Also: Fachbereich Physik, Freie Universität Berlin, Arnimallee 14, 14195 Berlin, Germany.

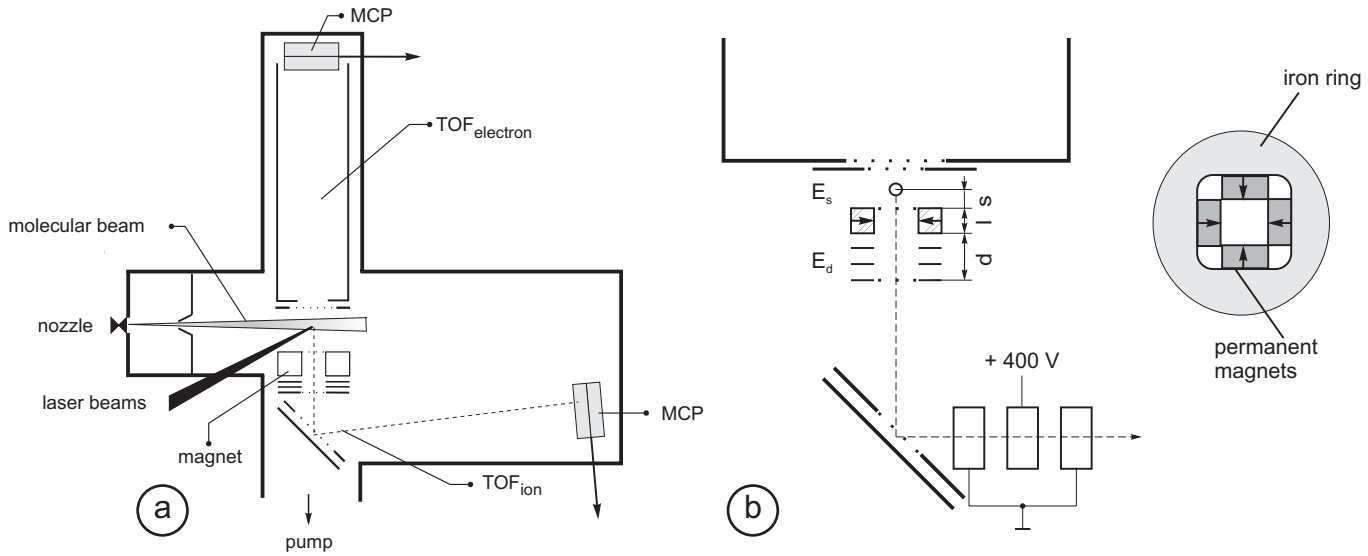

Fig. 1. (a) Scheme of the experimental set-up used in the photoelectron-photoion coincidence experiments. (b) Details of the ion and electron acceleration system and guiding system together with a schematic of the permanent magnet arrangement (shaded parts).

The photoelectron-photoion coincidence (PEPICO) technique is by now a well-established method when studying single photon ionization processes, *e.g.* with synchrotron radiation. It allows one to determine individual cluster ionization potentials as demonstrated for a variety of systems such as $(NH_3)_n$ [5] or Xe_n [6] and to obtain information on ionic reaction channels [7]. Clearly, no information on the excited state dynamics can be obtained in this way. In contrast, two photon pump-probe ionization with fs laser pulses – which reveals such insight into the dynamics – usually averages over all kinetic energies of the photoelectrons. However, resonantly enhanced multiphoton ionization (REMPI) experiments with pulsed lasers typically lead to many ionization events per laser pulse so that coincidence experiments do not provide additional information. Only if the number of ion pairs created in each laser pulse is significantly smaller than unity, a coincidence experiment allows one to correlate the electrons and ions detected with individual ionization and fragmentation processes.

We have used, for the first time, the pump-probe technique with fs laser pulses in combination with the coincidence detection method for the ions and electrons in order to study the dynamics of molecules and clusters on the fs time-scale. In the present paper we report a detailed description of this method and exemplify its potential by femtosecond time-resolved PES of ammonia molecules and clusters. Ammonia clusters are very interesting model systems for studying protonation and a variety of theoretical attempts have been made to approach the interaction potential and dynamics [8] for the smaller clusters. We use 140 fs laser pulses at the wavelength of 200 nm as pump photons. In this wavelength region the ammonia molecules and clusters are excited to vibrational levels of the electronic $\tilde{A}$ state which have been found to decay in a few 100 fs [9–12]. Ionization occurs with pulses at 400 nm or 267 nm. Preliminary results from this work have been reported previously [13,14]. The present paper describes in detail the experimental method and procedure and reports representative results for the NH_3^+ molecule, for $(NH_3)_2^+$ and for the protonated species $(NH_3)_{n-2}NH_4^+$ up to $n \leq 6$.

2 Experiment

A schematic of our experimental set-up is shown in Figure 1. Clusters are formed by supersonic expansion of ammonia (8%) seeded in He gas (1 bar) through a pulsed nozzle with a flat orifice (free jet expansion). Few experiments are conducted with a lower ammonia concentration (0.8%) resulting in a narrow cluster size distribution. A small contribution of benzene (0.1%) is added for calibration purposes. After passing the skimmer (1 mm) the molecular beam reaches the ionization region, where the molecules and clusters interact with the fs laser pulses of two weakly focused copropagating laser beams. The clusters are excited with a pump pulse (typical wavelength $\lambda_1 = 200$ nm) and ionized with a probe pulse ($\lambda_2 = 400$ nm or 267 nm) delayed by the time τ with respect to the pump pulse. The ions are detected by a time-of-flight (TOF) mass spectrometer while the simultaneously produced electrons are analyzed by a TOF electron spectrometer.

2.1 Laser system

The laser system used is a commercial Ti:sapphire laser and amplifier system (Clark MXR) tuned to a wavelength of 800 nm. The pulsed laser beam is split into two parts, one of which is transformed to the fourth harmonic by three successive BBO crystals [15] and is used to pump

the clusters. The second part of the laser beam is frequency doubled or tripled by one or two additional BBO crystals and is used to probe the excited clusters. The width (FWHM) of the laser pulses is about 140 fs. The laser fluences have to be strongly reduced to ensure ionization rates below 1 per pulse for the coincidence experiments. Typically, we use 5 μJ/cm^2 for the pump pulse and 40 μJ/cm^2 or 500 μJ/cm^2 for the probe pulse at the wavelength $\lambda_2 = 267$ nm or 400 nm. With these fluences we choose cluster concentrations in the beam such that the detected coincidence rate is well below 0.05 per laser pulse, thus optimizing the detection efficiency as discussed in Section 2.5. If the detected cluster ion signal decreases, as for example at larger time delays between pump and probe pulse, the laser pulse energies may be increased accordingly until a coincidence rate of 0.05 per pulse is reached again.

Hence, at a pulse repetition frequency of 1 kHz data acquisition times of 1 h are necessary to accumulate about 2×10^5 coincidences in the experiment. Since we are mainly interested in detecting cluster ions the monomer ion signal, which usually dominates the mass spectra in cluster experiments, has to be held as low as possible. In our experiments with a probe photon wavelength $\lambda_2 = 400$ nm this condition holds quite well since the total energy deposited into the system by one pump and one probe photon is $h\nu_1 + h\nu_2 = 9.3$ eV, which lies significantly below the NH_3 ionization potential ($IP = 10.18$ eV), *i.e.* at least two probe photons are needed for ionization of the initially excited $\widetilde{A}$ state.

2.2 TOF mass spectrometer

The time-of-flight (TOF) mass spectrometer is a modified Wiley-McLaren type spectrometer. In our double-field ion acceleration system the two accelerating regions (lengths s and d, see Fig. 1b) are separated by a field-free region (length l) into which the magnetic system of the electron spectrometer is inserted. Because of this variation the spatial focussing condition is slightly modified with respect to standard setup:

$$L = 2sk^{\frac{3}{2}}\left(1 - \frac{d/s}{k+\sqrt{k}} - \frac{l}{2s\sqrt{k}}\right)$$
$$\text{with} \quad k = 1 + \frac{E_d d}{E_s s}$$

with L being the length of the drift region (about 1 m) while E_d and E_s denote the field strengths in the ion and electron accelerating regions, respectively (Fig. 1b). The spatial focussing condition for the ions can be satisfied by changing the ratio E_d/E_s. In our arrangement we use $s = 0.5$ cm, $l = 1$ cm and $d = 2.5$ cm. Using 1000 V for the whole acceleration region the field strengths in the two accelerating regions are $E_d = 370$ V/cm and $E_s = 70$ V/cm. The accelerated ions are reflected by an ion mirror and directed to a MCP detector. In front of the detector an additional acceleration of the ions to 5 keV is possible. The divergence of the ion beam caused by the inhomogeneous magnetic field in the ionization region is corrected by an ion lens. The meshes used in the ion acceleration and detection system have a high transmission of about 96...98%.

2.3 Electron spectrometer

Our TOF electron spectrometer is a "magnetic bottle" type spectrometer [16]. The strong, inhomogeneous magnetic field at the ionization region is formed by four permanent magnets, which are fixed in an iron ring (Fig. 1b). All magnets are radially magnetized. The magnetic field strength in the ionization region thus created is about 1700 Gauß. In a distance of 10 mm it decreases to about 100 Gauß. An uniform, low field of about 3 G in the drift tube (with a length 0.6 m) is provided by a solenoid. This part of the spectrometer is shielded by μ-metal to prevent distortions of the magnetic field by earth field, electromagnetic pulses etc. In front of the MCP detector the electrons are postaccelerated to an energy of 300 eV.

Before the laser pulse is fired, a small accelerating field (about 1 V/cm) is applied to the ionization region. In this way even the very low energy electrons acquire a finite initial velocity so that contact potentials from different materials used may be neglected.

The calibration of the energy scale has been achieved with well-defined electron energies obtained by three-photon ionization of Xe at $\lambda = 256$ nm leading to an electron energy of 2.43 eV and by two-photon ionization ($\lambda_1 = 200$ nm and $\lambda_2 = 400$ nm) of benzene resulting in electrons of 60 meV energy. The energy resolution of the electron spectrometer depends on the energy detected (roughly proportional to $\sqrt{E_{el}}$). For low energy electrons it is about 30 meV whereas for 2 to 3 eV a value of about 100 meV has been observed.

2.4 Data acquisition

The electronics which allows us to detect coincidences between photoelectrons and photoions is depicted schematically in Figure 2. The key-device is a time-to-digital converter with the capability to register multiple events in two separate channels (multi-hit TDC, Le Croy model 4208). The ionizing laser pulse triggers the TDC. The extraction field E_s in the ion time-of-flight spectrometer is switched on with a small but constant delay (300 ns) to allow the photoelectrons to leave the extraction region. The photoions and electrons are detected by microchannel plates. The resulting signals are amplified and discriminated by two preamplifiers/discriminators (NOVOLEC AD100B). The NIM pulses are then fed into the two entrance channels of the TDC. Up to four events per channel can be registered with the TDC. Each event gives the time-of-flight of an ion or electron in the corresponding spectrometer. After a delay of several 100 μs with respect to the start pulse the complete dataset is transferred into a PC and

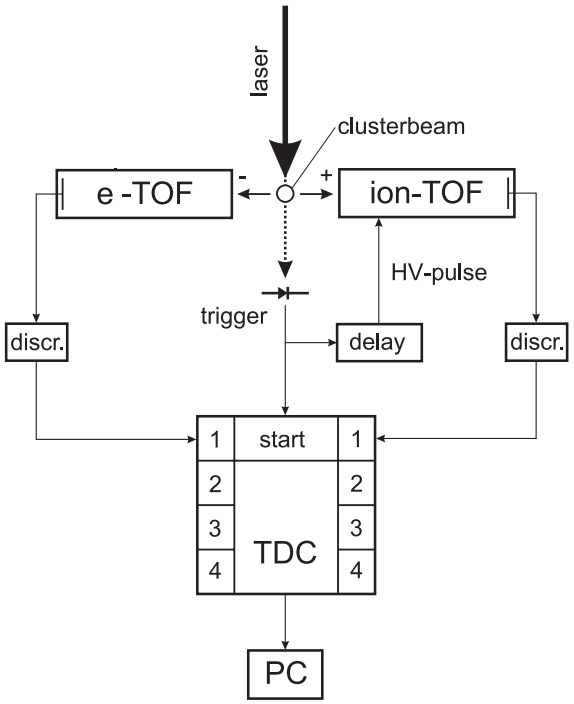

Fig. 2. Scheme of the electronics used to detect photoion-photoelectron coincidences. The key device is a multi-hit time-to-digital converter. For details see text.

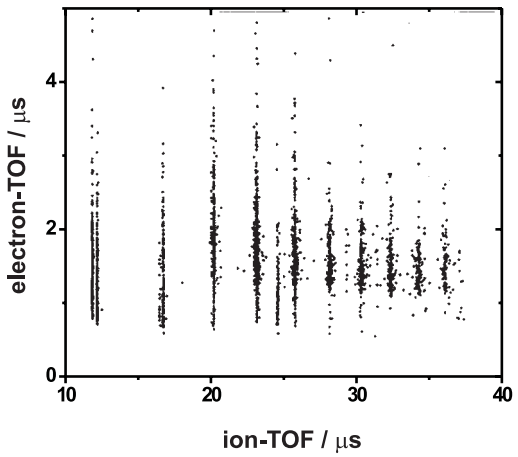

Fig. 3. Raw coincidence data as a function of the electron and ion time-of-flight for ammonia clusters excited with 200 nm and ionized with 400 nm. Each dot corresponds to a single coincidence event. One clearly identifies different masses (vertical lines) with their individual, different electron spectra.

the TDC is cleared for the next measuring cycle initiated by the subsequent laser pulse.

The raw data are analyzed and stored by a data acquisition program running on the PC. A *relevant coincidence event* is characterized by *one pulse being detected in the electron channel and one in the ion channel* within a reasonable time interval, which is essentially given by the maximum time-of-flight of any ion expected. All other events are not stored as coincidences. The coincidence events are accumulated in a two-dimensional array, relating them to the electron and ion time-of-flight. An example is shown in Figure 3 for ammonia clusters excited with 200 nm pump pulses and 400 nm probe pulses. In addition, all events counted in the electron and ion channel, including those with either none or more than one event in the other detection channel, are stored in two additional one-dimensional arrays, representing the integral mass and electron spectra, respectively.

2.5 Optimization of the coincidence rates

As already mentioned, in order to detect predominantly true coincidences it is necessary to keep the signal rate very low (*e.g.* by reducing the laser pulse energy) so that the mean number $\bar{n}$ of electron-ion pairs produced per laser pulse is small, $\bar{n} \ll 1$. We will now elaborate on this statement quantitatively. Assume that all electrons and ions detected arise from photoionization processes in the course of which one electron and one ion (possibly a fragment) are created. Both species suffer some losses on the way to detection, *e.g.* at the field defining meshes, by collisions with the rest gas and an efficiency of less than unity for the multichannel plate detectors. The number of ions and electrons detected is

$$w_i = \xi_i \bar{n} \tag{2}$$

$$\text{and } w_e = \xi_e \bar{n} \tag{3}$$

with ξ_i and $\xi_e < 1$ accounting for the finite detection probability for the ions and electrons, respectively.

Under stable experimental conditions, *e.g.* constant cluster concentration and laser pulse energies, the number n of electron-ion pairs produced per pulse can be described by a Poisson distribution for the probability p_n to observe n pairs after one laser pulse:

$$p(n) = \frac{\bar{n}^n}{n!} e^{-\bar{n}} \,. \tag{4}$$

If n electrons (ions) are created by a laser pulse the probability to detect k of them is given by the binomial distribution:

$$p_{e(i)}(n,k) = \binom{n}{k} \xi_{e(i)} (1 - \xi_{e(i)})^{n-k}. \tag{5}$$

The probability w_{11} of detecting exactly one electron and one ion simultaneously is thus given by summing the product $p_e(n,1)p_i(n,1)p(n)$ over all n:

$$w_{11} = \xi_i \xi_e \bar{n} [1 + \bar{n}(1 - \xi_e)(1 - \xi_i)] \times \exp\left\{-\bar{n} + \bar{n}\,(1 - \xi_i)\,(1 - \xi_e)\right\}. \tag{6}$$

This is the total number of coincidences detected per laser pulse which contains true coincidences (belonging to an electron-ion pair from the same event) and false coincidences (ion and electron arise from different events).

Table 1. Determination of ξ_e, ξ_i and $\overline{n}$.

number of counts				from this follows		
total	coinc.	electr.	ions	ξ_i	ξ_e	$\overline{n}$
500 000	12 834	42 100	29 650	0.36	0.50	0.17
200 000	9 466	30 902	27 466	0.43	0.48	0.32
200 000	4 955	16 500	14 100	0.36	0.42	0.20
500 000	12 834	35 810	29 650	0.41	0.49	0.15

In contrast, out of n pairs created in a laser pulse the probability to detect one electron and one ion which belong to the same pair is $1/n$ so that $p_e(n,1)p_i(n,1)p(n)/n$ true events are detected in this case. After summing over all n we finally obtain the average number of *true coincidences* per pulse:

$$w_{11}^{(t)} = \xi_i \xi_e \bar{n} \exp\left\{-\bar{n} + \bar{n}\left(1-\xi_i\right)\left(1-\xi_e\right)\right\}. \qquad (7)$$

As a function of the average number of ionization events per pulse $\bar{n}$ (electron-ion pairs produced) the number of true coincidences per laser pulse reaches a maximum

$$w_{11}^{max} = \xi_i \xi_e e^{-1}\left[1-\left(1-\xi_i\right)\left(1-\xi_e\right)\right]^{-1}$$

for $\bar{n}_{max} = \left[1-\left(1-\xi_i\right)\left(1-\xi_e\right)\right]^{-1}$.

On the other hand, the average number of *false* (uncorrelated) *coincidences* per laser pulse – resulting from the simultaneous detection of one electron with any ion but not the correlated one – is given by subtracting equation (7) from equation (6):

$$w_{11}^{(f)} = \xi_i \xi_e \bar{n}^2 \left(1-\xi_i\right)\left(1-\xi_e\right) \times \exp\left\{-\bar{n} + \bar{n}\left(1-\xi_i\right)\left(1-\xi_e\right)\right\}. \qquad (8)$$

Clearly, no false coincidences are detected ($w_{11}^{(f)} = 0$) if one of the detection efficiencies is unity (we recall at this point, see Sect. 2.4, that we register only those events as coincidences where exactly one ion and one electron are detected and we reject all data with more than one event in either channel). Thus, the higher the detection efficiencies ξ_e and ξ_i, the higher a mean number $\bar{n}$ of electron-ion pairs can be tolerated to ensure a constant, acceptable small fraction of uncorrelated coincidences.

Experimentally, we can determine the total numbers of ions w_i (Eq. (2)), electrons w_e (Eq. (3)) and coincidences w_{11} (Eq. (6)) per laser pulse. Thus, with the help of these three equations we may derive the experimental parameters ξ_i, ξ_e and $\bar{n}$.

A typical set of data is shown in Table 1. These data were measured on different days with slightly different adjustment and different experimental parameters, hence the fluctuations of $\xi_i$and ξ_e.

The dependence of total (w_{11}), true ($w_{11}^{(t)}$) and false ($w_{11}^{(f)}$) coincidence rates on the average number of events ($\bar{n}$) per laser pulse according to equations (6–8) is shown in Figure 4. Here we have used typical values for the ion and electron detection efficiencies, $\xi_i = 0.4$ and $\xi_e = 0.45$, respectively. The rate of true coincidences peaks at $\bar{n} = 1.5$.

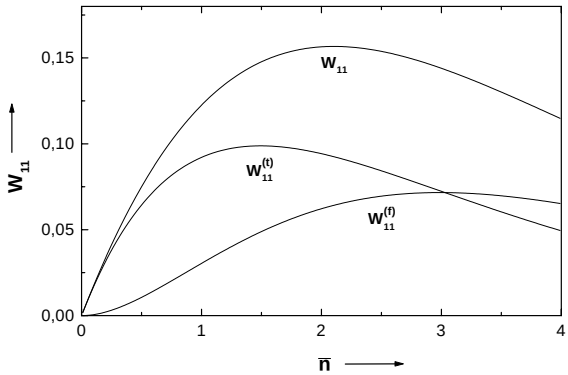

Fig. 4. True ($w_{11}^{(t)}$), false ($w_{11}^{(f)}$) and total ($w_{11} = w_{11}^{(t)} + w_{11}^{(f)}$) coincidence rates per laser pulse as function of the mean number $\bar{n}$ of ion-electron pairs per laser pulse. The detection efficiency for ions and electrons is $\xi_i = 0.4$ and $\xi_e = 0.45$, respectively.

At this point the rate of false coincidences is relatively high, being about one third of the total coincidence rate. The ratio $w_{11}^{(t)}/w_{11}^{(t)} + w_{11}^{(f)}$ has its largest value at small numbers $\bar{n}$. The contribution of uncorrelated coincidences to the electron spectrum of the mass of interest could be eliminated approximately by subtracting a corresponding fraction of the total electron spectrum. This, however, implies a completely statistical appearance of false coincidences, *i.e.*, the energy distribution of uncorrelated electrons is identical to the energy distribution of the total electron signal obtained as the sum over all electrons registered for the complete mass spectrum. To minimize errors from such an approximative procedure, in our experiments we have kept the signal rate below $\overline{n} = 0.3$ for the mean number of electron-ion-pairs created in the ionization process. According to equations (6, 8) this leads to a total coincidence rate of less than 0.05 per pulse from which less than 1/10 are false coincidences. Due to this reason the correction of the experimental results discussed in the following is not necessary.

3 Results and discussion

3.1 NH_3

Figure 5 shows a typical coincidence mass spectrum obtained without time delay between the pump pulse at $\lambda_1 = 200$ nm and the probe pulse at $\lambda_2^{(1)} = 400$ nm. The zero time delay is defined by the benzene signal registered simultaneously (*cf.* Fig. 5). Displayed here are the coincidences accumulated over 3×10^5 pulses and integrated at each ion time-of-flight over all electron energies. The ammonia monomer signal which usually dominates the observed cluster distribution is relatively small because two probe photons are necessary for ionization. Hence, the observed coincidence spectrum emphasizes the ammonia clusters, facilitating their observation with a sufficiently high signal strength. Nevertheless the monomer

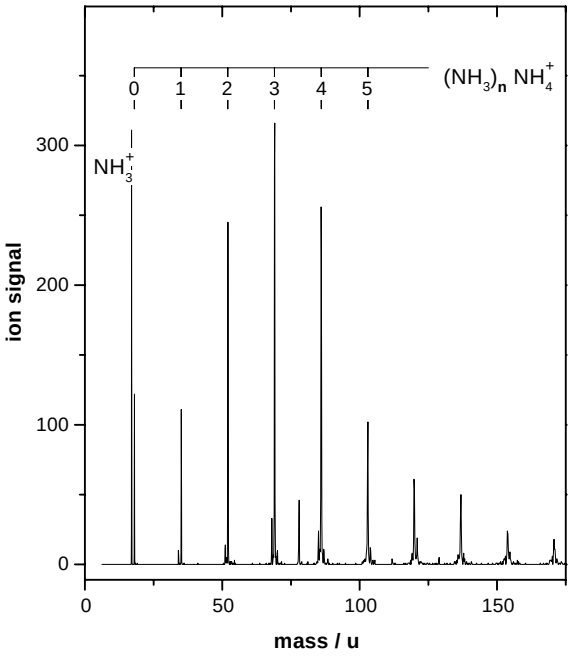

Fig. 5. Coincidence mass spectrum of $(NH_3)_n NH_4^+$ cluster ions without time delay between the pump pulse at 200 nm and the probe pulse at 400 nm (for NH_3, $(NH_3)_2$, and NH_4 two probe photons are necessary for ionization [12]).

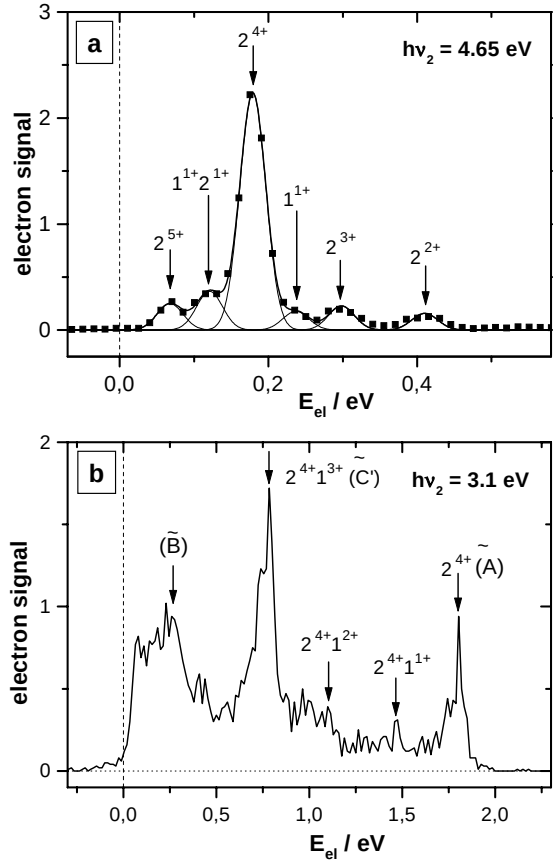

Fig. 6. Coincidence photo-electron spectra of NH_3^+ at the delay time $\tau = 0$ for ionization with one probe photon of 4.65 eV (a) and two photons of 3.1 eV (b).

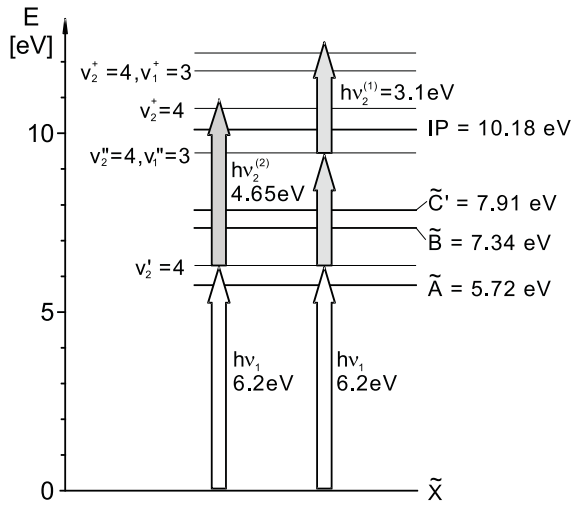

Fig. 7. Schematic of the energy levels for the NH_3 molecule, showing the photon energies used in the two different pump-probe schemes.

signal is strong enough for a detailed analysis of coincidence electron spectra obtained with either $\lambda_2^{(1)} = 400$ nm or $\lambda_2^{(2)} = 267$ nm. The measured spectra for the zero time delay are presented in Figure 6.

They are characterized by discrete narrow lines which can be assigned unambiguously by virtue of a strong Franck-Condon relation ($\Delta v = 0$) between the vibrationally excited levels in the $\tilde{A}$ and in the $\tilde{X}$–ion state due to their nearly identical planar geometry. The energetics of the system is depicted in Figure 7 showing that at a pump wavelength $\lambda_1 = 200$ nm the ammonia molecule is excited nearly resonantly to the $v_2' = 4$ level of the ν_2' umbrella mode in the electronic $\tilde{A}$ state (*cf.* [17]). Hence, the transition to the $v_2^+ = 4$ level in the ionic state dominates the electron spectrum as, indeed, confirmed by the measured spectra (Fig. 6). Probing with a wavelength $\lambda_2^{(2)} = 267$ nm (Fig. 6a) leads to the dominant peak at $E_{el} \sim 0.2$ eV belonging to an internal ion energy of 0.45 eV (see Fig. 7). The satellite peaks in Figure 6a are identified as neighboring harmonic and combination bands of the ν_2^+ out-of-plane bending mode and the ν_1^+ symmetric stretch mode. The vibrational mode energies obtained of $h\nu_2^+ \approx 0.11$ eV and $h\nu_1^+ \approx 0.39$ eV agree within our experimental resolution very well with corresponding literature values [4]. The photo-electron spectrum confirms again the energy calibration of our spectrometer. The measured energy resolution of 40 meV (see Fig. 6a) agrees well with the estimated spectrometer resolution of about 30 meV (given in Sect. 2.3) broadened by the spectral width of the 140 fs laser pulse (12 meV).

When probing with a wavelength $\lambda_2^{(1)} = 400$ nm, two probe photons with $h\nu_2^{(1)} = 3.1$ eV are needed for ionization (Fig. 7) leading to an excess energy in the ionic state which is 1.55 eV higher than for $h\nu_2^{(2)} = 4.65$ eV. Consequently the $4\nu_2^+$ excitation in the ionic state leads

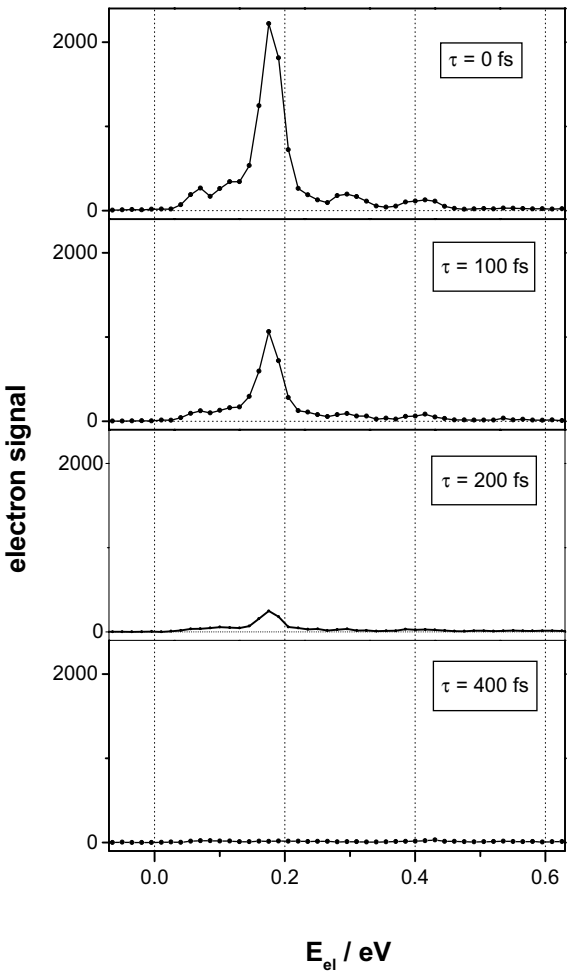

Fig. 8. Electron spectrum of NH_3^+ for different delay times τ between the pump pulse at 200 nm and the probe pulse at 267 nm.

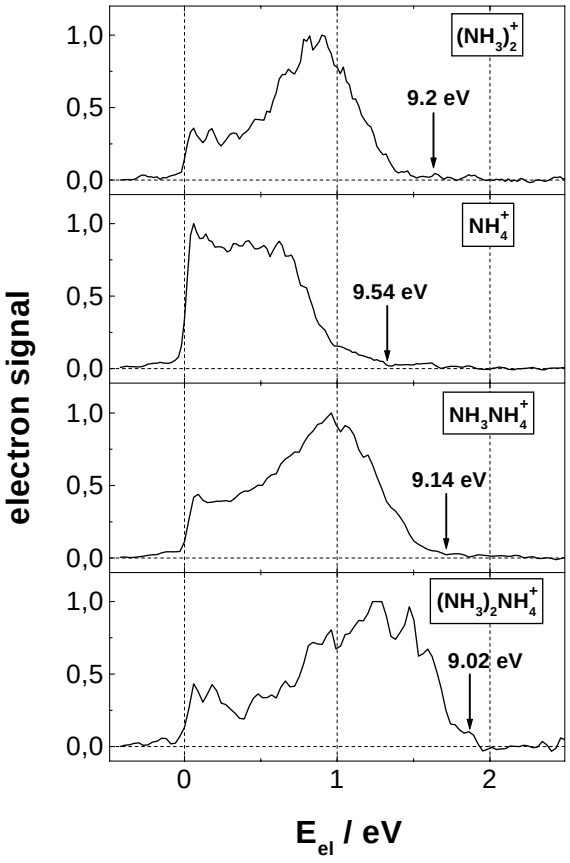

Fig. 9. Coincidence electron spectra (normalized) of ammonia clusters (narrow cluster size distribution) for $\tau = 0$ at $\lambda_1 = 200$ nm and $\lambda_2^{(2)} = 267$ nm. The energy values at the arrows represent the appearance potentials of the corresponding cluster ions.

now to an electron energy of $E_{el} \sim 1.75$ eV. The peaks at lower electron energies in Figure 6b correspond to higher internal energies in the ammonia ion and reflect vibronic excitation in the $\tilde{B}$ and $\tilde{C}'$ electronic state of ammonia due to absorption of the first probe photon (see Fig. 7). The strong peak at $E_{el} = 0.75$ eV, for example, arises probably from excitation of the $v_2'' = 4$, $v_1'' = 3$ combination band in the $\tilde{C}'$ state with the second (the ionizing) probe photon leading into the corresponding energy levels of the ionic ground state. The structure at $E_{el} = 0.25$ eV in the ammonia electron spectrum of Figure 6b reflects the higher internal ion energy resulting from the higher vibrational excitation in the electronic $\tilde{B}$ state by the first probe photon.

The ammonia electron spectrum displayed in Figure 6 for zero delay time rapidly disappears for small delay times $\tau > 0$, as shown in Figure 8 for $\lambda_2^{(2)} = 267$ nm. The lifetime of NH_3 excited to the $v_2' = 4$ level of the state has been found to be in the order of 40 fs [10] and a signal at $\tau = 200$ fs is observed only because of the finite width of our laser cross correlation curve. Despite this very short lifetime the photoelectron spectroscopy with fs laser pulses has enabled us to obtain the complete information about the energy balance of the ammonia molecule after excitation to the fast decaying vibronic states.

3.2 $(NH_3)_n$

In Figure 9 the coincidence electron spectra of the clusters $(NH_3)_n$ at $\tau = 0$ are given for the probe wavelength $\lambda_2^{(2)} = 267$ nm. The maximum possible electron energy for each cluster ion

$$E_{el}^{max} = h\nu_1 + h\nu_2 - AP \tag{9}$$

is derived from the respective appearance potentials AP and is marked by arrows in Figure 9 (the values given there and in the following figures represent the AP taken from earlier synchrotron radiation experiments [5]). Except for $(NH_3)_2^+$, the electron energies are distributed over the whole accessible energy range. Note that low electron energy E_{el} corresponds to high internal ion energy E_{ion} (see Eq. (1)). Because of the high density of vibronic cluster states no discrete structures can be observed in the electron spectra. The protonated ions $(NH_3)_{n-2}NH_4^+$

are formed by NH_2 loss from the parent $(NH_3)_n^+$ cluster ions, hence the smaller maximum electron energy for NH_4^+ as compared to $(NH_3)_2^+$. The electron spectrum of $(NH_3)_2^+$ strongly decreases for low electron energies E_{el} (high E_{ion}) since there fragmentation of the highly excited ions is dominant and leads to an enhanced electron signal in the fragment ion channel NH_4^+. The residual signal at low electron energies of $(NH_3)_2^+$ indicates that despite the high internal energy no complete fragmentation occurs during the long residence time (a few 100 ns) in the extraction zone. Partially the internal energy will be concentrated in the intramolecular vibrations with a relatively weak coupling to the intermolecular modes. In contrast, for the highest electron energies (small E_{ion}) in the $(NH_3)_2^+$ case the signal is very low. This may be due to small Franck-Condon factors due to the vibrational excitation of about 0.4 eV in the $\tilde{A}$ state similarly to the NH_3 monomer which indicates that no vibrational relaxation occurs within the dimer in the $\tilde{A}$ state during the laser pulse. It is interesting to note that even in the case of NH_4^+ the signal at the high electron energy end of the spectrum (between ∼1 and 1.3 eV) is weak: the system prefers apparently to remain $(NH_3)_2^+$ for these low internal energies even though fragmentation would be energetically possible. This restriction appears, however, to be somewhat relaxed as the cluster size gets larger, reflecting the observation of early dynamical studies [8] that $(NH_3)_2^+$ is much more robust against even internal protonation than *e.g.* $(NH_3)_3^+$. A detailed time dependent study of photoelectron spectra for $(NH_3)_2^+$ and NH_4^+ will be presented in a forthcoming paper.

For all clusters shown in Figure 9 we have also studied the dependence of the photoelectron spectra on the delay time between the exciting pump and the probe pulse. As an example the time development of the electron spectrum for the $NH_3NH_4^+$ cluster ion is given in Figure 10. The pronounced maximum of the electron energy distribution for $\tau = 0$ at an electron energy of about 1 eV, *i.e.* at an internal ion energy of about 0.7 eV, reflects probably the vibrational excitation of $(NH_3)_3$ in the $\widetilde{A}$ state. This excitation decays very fast within about 200 fs [10] leading to the rapid drop of the maximum in the electron spectrum (Fig. 10).

In our earlier work we have described the dynamics of ammonia clusters in the electronically excited $\widetilde{A}$-state by a simple kinetic model which is illustrated schematically in Figure 11 [10]. In this picture, the ultrafast decay is caused mainly by fragmentation into the main loss channel as well as into the fragment state (4) and by rearrangement leading to the state (3). Both states for $(NH_3)_3$ are populated within the decay time of 200 fs (see Fig. 10) but have relatively long lifetimes of a few ps for state (3) and some μs for state (4) [10]. Hence, the broad and nearly constant contribution in the electron spectra is probably caused by probing the cluster states (3) and (4) reflecting their internal energy distribution.

The electron spectra at larger delay times (*e.g.* $\tau =$ 4 ps) are dominated by the contribution of the state (4),

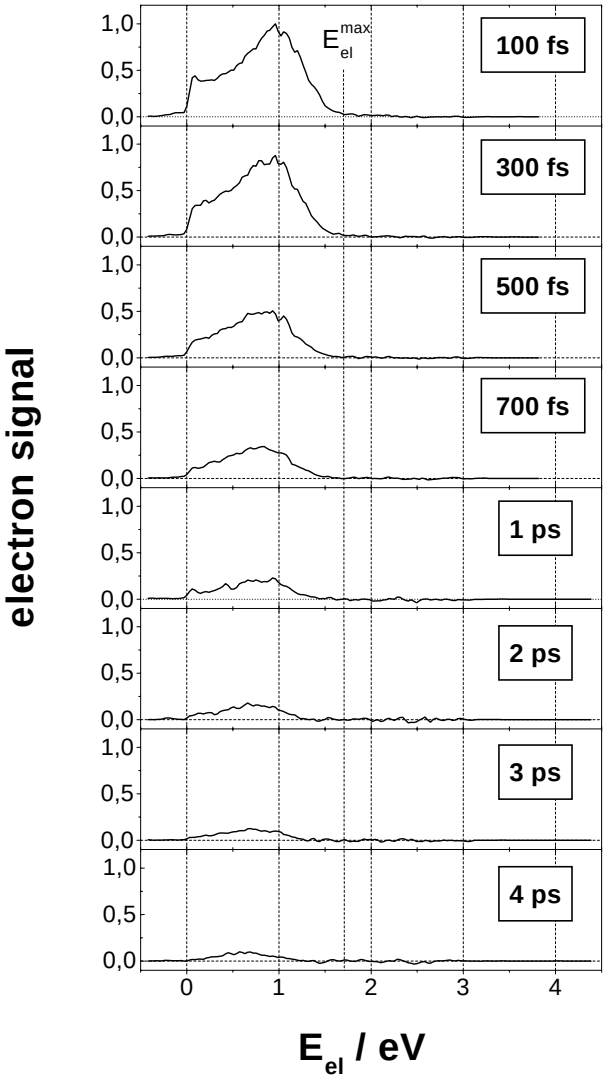

Fig. 10. Coincidence electron spectra of $(NH_3)NH_4^+$ for $\lambda_1 =$ 200 nm and $\lambda_2^{(2)} = 267$ nm for different delay times τ (narrow cluster size distribution).

i.e. by ionization of the radical NH_3NH_4 obtained after fragmentation (NH_2 ejection) of the neutral trimer $(NH_3)_3$ in the primarily excited $\tilde{A}$ state (2). Thus, the observed distribution allows one to determine the excitation energy of the neutral fragment NH_3NH_4. The difference between the probe photon energy of 4.65 eV and the ionization potential of 3.9 eV [18] for NH_3NH_4 is 0.75 eV. Thus the measured electron energies up to 1.2 eV (Fig. 10) indicate a maximum excitation energy of about 0.45 eV in the radical NH_3NH_4 after the fragmentation.

For the study of larger ammonia clusters we have taken advantage of their enhanced signal strength at the probe wavelength $\lambda_2^{(1)} = 400$ nm (see above). In Figure 12 the coincidence electron spectra of $(NH_3)_nNH_4^+$, $n = 2$, 4 are compared for delay times $\tau = 0$ and $\tau = 4$ ps. At zero delay time the electron spectra reach from zero up to the limit given by the appearance potentials (marked with the arrow and taken from [5]). The small electron signals

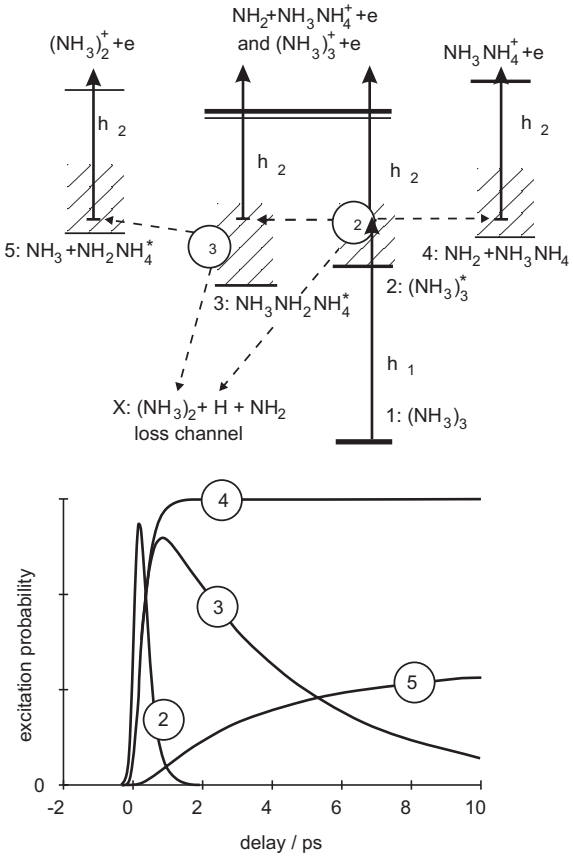

Fig. 11. Kinetic model for the dynamics of ammonia clusters, demonstrated, as example, for the trimer excited with $h\nu_1 = 6.2$ eV photons and probed with $h\nu_2 = 3.1$ eV photons. τ_2 and τ_3 represent the lifetimes of the excited states (2) and (3), respectively. In the lower part the typical time evolution of the population of the excited states (2–5) is shown. The kinetics for larger clusters is analogous.

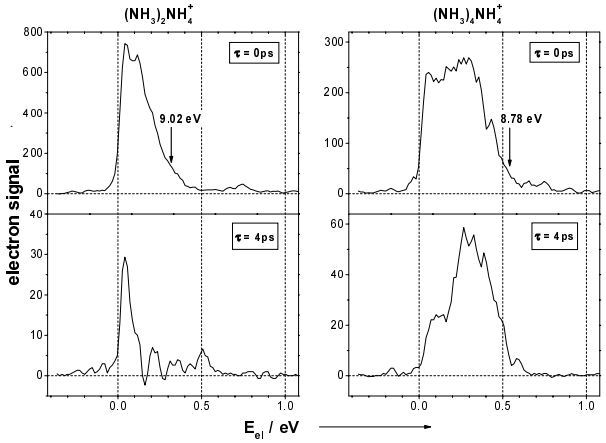

Fig. 12. Coincidence electron spectra of $(NH_3)_nNH_4^+$, $n = 2$, 4, for delay times $\tau = 0$ respective $\tau = +4$ ps between the pump pulse at 200 nm and the probe pulse at 400 nm (the energy values at the arrows represent the appearance potentials).

above the upper limit may be due to a weak contribution caused by two probe-photon absorption at the relatively high fluence of the probe beam. The electron signals at $\tau = 4$ ps are much smaller than for $\tau = 0$ as can be seen by comparing the scales on the respective ordinates. For $(NH_3)_2NH_4^+$ the particularly weak signal at $\tau = 4$ ps is limited to about $E_{el} = 0.1$ eV. As known from earlier experiments [12] the signals at $\tau = 4$ ps are formed predominantly by the ionization of the neutral fragments (corresponding to state (4) in Fig. 11) with probe photons of 3.1 eV energy. Then we conclude for $(NH_3)_2NH_4^+$ with the ionization potential $IP = 3.3$ eV [18] that this fragment is formed with an excitation energy up to 0.3 eV. For $(NH_3)_4NH_4^+$ with $IP = 2.73$ eV, we derive from the corresponding electron spectrum (Fig. 12) nearly the same maximum excitation energy of 0.3 eV for the fragment. For this cluster a significant signal reduction is found for the small electron energies (see Fig. 12), *i.e.* for the higher E_{ion}. The transitions from the highly excited states of $(NH_3)_nNH_4^*$ initiated by the 3.1 eV probe photons lead to ionic states with an internal energy which is the higher the smaller the ionization potentials are. The Franck-Condon factors for these transitions will decrease remarkably if the geometries in the excited and the ionic cluster fragment state differ not too strongly. The signal reduction at low electron energies of $(NH_3)_4NH_4^+$ is caused by its lower ionization potential resulting in the larger excess energy in the ionic state with a lower Franck-Condon transition probability to the higher lying ion levels. A more detailed analysis of the electron energy distribution for the ammonia cluster fragment ions requires much more information about the spectra and potential curves of the corresponding cluster fragment states.

4 Conclusion

We have shown that fs-pump-probe technique with 1 kHz laser systems can be combined with time-of-flight photoelectron spectroscopy for neutral clusters by coincident detection of photo-ions and -electrons. A detailed analysis of the optimal experimental conditions shows that one should keep the average number of events per laser pulse below 0.05. The time resolved photoelectron spectra related to various protonated and unprotonated ammonia cluster ions allow one in principle to obtain very deep insights into the excited state dynamics. A thorough understanding warrants, however, intensified theoretical investigations into potential energy surfaces, Franck-Condon factors and an effort to model the dynamics of protonation and fragmentation, at least for some of the smaller cluster systems. To predict the observed photoelectron spectra and their time evolution is a strong challenge for modern quantum dynamical theory.

Financial support by the Deutsche Forschungsgemeinschaft through Sonderforschungsbereich 337 is gratefully acknowledged.

References

1. *Femtosecond Chemistry*, edited by J. Manz, L. Wöste (Verlag Chemie, Weinheim, 1995).
2. B.J. Greenblatt, M.T. Zanni, D.M. Neumark, Science **276**, 1675 (1997).
3. D.R. Cyr, C.C. Hayden, J. Chem. Phys. **97**, 771 (1996).
4. M.R. Dobber, W.J. Buma, C.A.D. Lange, J. Chem. Phys. **99**, 1671 (1995).
5. W. Kamke, R. Herrmann, Z. Wang, I.V. Hertel, Z. Phys. D **10**, 491 (1988).
6. L. Cordis, G. Ganteför, J. Hässlich, A. Ding, Z. Phys. D **3**, 323 (1986).
7. C. Dedonder-Lardeux, I. Dimicoli, C. Jouvet, S. Matrenchard-Barra, M. Richard-Vicard, D. Solgadi, M. Vervloet, Chem. Phys. Lett. **240**, 97 (1995).
8. J.C. Greer, R. Ahlrichs, I.V. Hertel, Z. Phys. D **18**, 413 (1991).
9. J. Purnell, S. Wei, S.A. Buzza, A.W. Castleman, J. Phys. Chem. **97**, 12530 (1993).
10. T. Freudenberg, W. Radloff, H.-H. Ritze, V. Stert, K. Weyers, F. Noack, I.V. Hertel, Z. Phys. D **36**, 349 (1996).
11. K. Fuke, R. Takasu, Bull. Chem. Soc. Jpn **68**, 3309 (1995).
12. T. Freudenberg, W. Radloff, H.-H. Ritze, V. Stert, F. Noack, I.V. Hertel, Z. Phys. D **41**, 267 (1997).
13. W. Radloff, V. Stert, T. Freudenberg, I.V. Hertel, C. Jouvet, C. Dedonder-Lardeux, D. Solgadi, Chem. Phys. Lett. **281**, 20 (1997).
14. V. Stert, W. Radloff, T. Freudenberg, F. Noack, I.V. Hertel, C. Jouvet, C. Dedonder-Lardeux, D. Solgadi, Europhys. Lett. **40**, 515 (1997).
15. J. Ringling, O. Kittelmann, F. Noack, G. Korn, J. Squier, Opt. Lett. **18**, 2925 (1993).
16. P. Kruit, F.H. Read, J. Phys. E **16**, 313 (1983).
17. V. Vaida, M.I. McCarthy, P.C. Engelking, P. Rosmus, H.J. Werner, P. Botschwina, J. Chem. Phys. **86**, 6669 (1987).
18. K. Fuke, R. Takasu, F. Misaizu, Chem. Phys. Lett. **229**, 597 (1994).